

A Coefficient Clustering Analysis for Damage Assessment of Composites based on Pulsed Thermographic Inspection

Yifan Zhao^{*}, Lawrence Tinsley, Sri Addepalli, Jörn Mehnert, Rajkumar Roy

EPSRC Centre for Through-life Engineering Services, Cranfield University, Cranfield, MK43 0AL, UK

^{*} Corresponding author. Tel.: +44(0) 1234750111 Ext 2283; fax: +44(0) 1234758292. *E-mail address*:

yifan.zhao@cranfield.ac.uk

Abstract

This paper introduces a coefficient clustering analysis method to detect and quantitatively measure damage occurring in composite materials using pulsed thermographic inspection. This method is based on fitting a low order polynomial model for temperature decay curves, which a) provides an enhanced visual confirmation and size measurement of the damage, b) provides the reference point for sound material for further damage depth measurement, c) and reduces the burden in computational time. The performance of the proposed method is evaluated through a practical case study with carbon fibre reinforced polymer (CFRP) laminates which were subjected to a drop impact test with varying energy levels. A novel method for reducing an entire thermogram sequence into a single image is introduced, which provides an enhanced visualisation of the damage area.

Highlights

- A coefficient clustering analysis method to assess damage in composite materials is proposed.
- Distribution of estimated coefficients provides an alternative to characterise damage.
- This technique not only provides an enhanced visual confirmation of the damage, but also reduces the burden on the operator in post-processing the data.
- Improvement to suitability of pulsed thermography to assess impact damage in composites.

Keywords

NDT; Thermography; Impact damage assessment; Delamination

1. Introduction

Composite materials are well known for their high strength-to-weight ratios, low density and corrosion resistant properties in comparison with traditional metallic components. As such, they are applied in a wide variety of contexts, increasingly in automotive and aerospace sectors; where there is a huge requirement to improve system performance through weight reduction. With the rising price of aviation fuel and attitude towards environmental issues, modern aircraft manufacturers are looking out for innovative solutions that can offer better performance without compromising the structural integrity and safety features of the aircraft. Thus the current generation of aircrafts are seeing large introduction of composite components that constitute to about 50% by weight of the aircraft in parts such as engine casings, wing sections, tail plane, control structures and fuselage [1]. However, composites are also well known for their vulnerability to impact damage and their difficulty to repair compared to metal based components. An impact or strike on the surface may cause structural damage that may be exhibited with only a small surface visual profile – this is known as barely visible impact damage (BVID) [2]. Even though the damage is ‘barely visible’ on the surface, the damage to the structure could severely affect its properties and performance, which may not be apparent from the surface profile of the impact.

A variety of impact sources exist, such as stones, hail, bird strike and even accidental drop of workmen tools during maintenance that can cause impact damage. Literature suggests that bird strikes account for up to 80% of service damage to composites in the aerospace sector [3]. While the surface may appear sound, there may be significant damage hidden in the internal structure, and may not be appreciated on the surface because of a difficult relationship between appearance of surface features and structural integrity of the part [4, 5]. When the composite structure is subjected to a minor impact damage that is barely visible on

the surface, the damage even at the micro scale can progress to significant structural damage that affects the strength, durability and stability of the composite laminates [6].

In the aviation industry, multiple non-destructive testing or NDT methods are employed, ranging from direct visual inspection, dye-penetrant, magnetic particle, eddy current, radiography to advanced methods such as 3D computed tomography, ultrasound and thermography to capture the health and structural integrity of the component without creating or intensifying any further damage to the component that is being inspected. This diversity of inspection methods requires a range of skills and expertise, providing results with differing margins of error between them.

Thermography has been attracting increasing attention over recent decades as the method involves a rapid, robust, non-contact, non-invasive inspection. Thermography can be divided into two modes: passive and active. The passive mode applies where deviations from normal operation exhibit a change in thermal contrast to be observed by an infrared imager, while active thermography involves the input of an external heat that generates a measurable thermal contrast. This particularly applies where an inspected part is not in use and is in thermal equilibrium with its surrounding environment, when detection of sub-surface damage and defects is sought, or for the measurement of material thermo-physical properties. In order to generate a thermal contrast, heat input is designed to highlight damages and defects either using them to generate the heat signal, as in the case of vibro-thermography, or as an obstruction or conduit to heat flow. Thermography in its varied forms has found applications in many contexts such as condition monitoring of electrical equipment [7], mechanical equipment [8], welds [9], structures [10], and aerospace composites [11, 12] and Through-Life Engineering [13].

In infrared thermography, various image processing methods are in common use, from the basics of dealing with fixed pattern noise, vignetting, bad pixels and spatial noise smoothing

[14], to thermal contrast algorithms [15] which have been further developed over the years [16]. The Thermographic Signal Reconstruction (TSR) [17] algorithm was a landmark development in pulsed thermography which dramatically increased spatial and temporal resolution of a thermogram sequence and opened up the opportunity for new ways of processing pulsed thermography data. Others have applied Principal Component Analysis (PCA) to thermography, also referred to as Principal Component Thermography (PCT), on TSR coefficients that improved the results from typical averaging filters, with comparable results to Pulse-Phase Thermography [18]. PCA analysis has also been applied to a TSR-type treatment of per-pixel signal data [19] in order to differentiate different delamination sizes and lengths, with sensitivity to delamination opening. Additional study has involved use of skewness parameter [20], and high order statistics, with somewhat consistent performance in signal-to-noise ratio for defects of different size and depth [21]. TSR based analysis processes have previously been explored with exciting developments, involving the transformation of the thermography data into a series of RGB colour images synthesized from TSR polynomial coefficients [22]. The data thus obtained may be plotted for each colour shade to estimate contrast emergence times together with depth scaling, and has been applied to both artificial and real damage features [23]. This specific application has been proven to be quite powerful at extracting multiple features into single images.

This paper is limited to focus on damage detection and corresponding sizing measurement with an application in assessing degradation caused by drop impact. Damage detection is important because a number of commonly used feature depth measurement methods, such as Peak Temperature-Contrast [15] and Peak Temperature-Contrast Slope [24], often require a reference point that is known on a sound material. Ringermacher [24] used the average temperature from the entire surface before flash as reference. This can work well only when the defective region is small and the surface is uniformly illuminated. Curve-fitting based

methods, such as Shepard's Peak Second-derivative method [25] and Sun's Least-Squares Fitting method [26, 27] require fitting either a high order polynomial model or a complex heat diffusion model. A high order polynomial model can experience the over-fitting problem when the model has too many parameters relative to the number of observations, especially when the data is noisy. Although fitting based on a physical model (the model structure being known) reduces the sensitivity to noise, it requires multiple unknown parameters to be estimated simultaneously using optimisation techniques. However, this can be very time-consuming and sometimes only locally optimal solutions are produced rather than globally optimal solutions. Developing a fast, automatic and reliable technique with high robustness against noise for damage detection is therefore a key goal of the community.

2. Experimental data

2.1 Specimen

Specimens were produced with the dimension of 150mm x 100mm x 4mm, which were made of unidirectional Toray 800 carbon fibres pre-impregnated with Hexcel M21 epoxy resin. The laminates were subjected to a drop impact test with predefined energy levels using a semi-

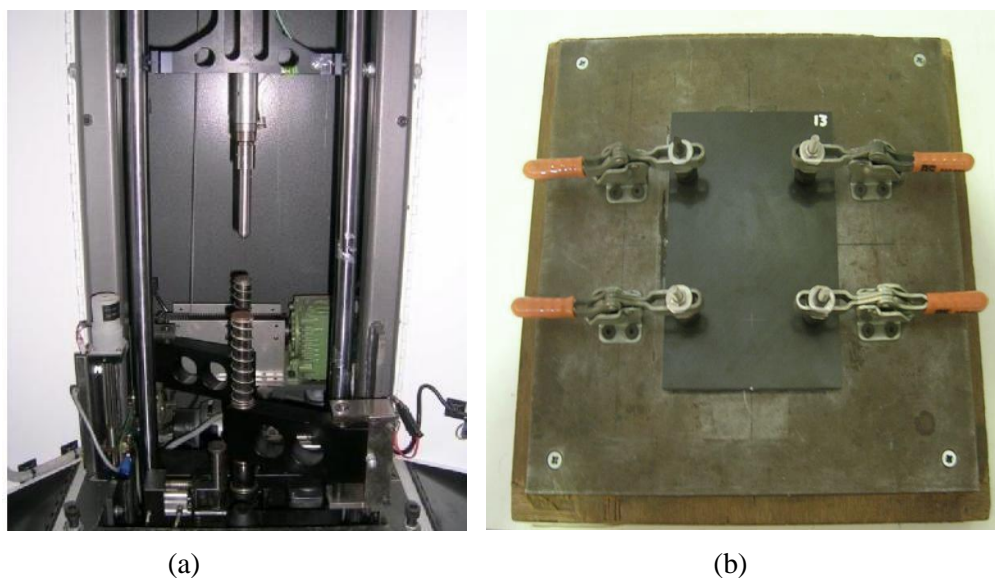


Fig. 1: (a) The weight-drop machine used for impact generation and (b) specimen support fixture.

spherical 16mm diameter weight drop machine which employed a drop weight of 2.281kg, as illustrated in Fig. 1(a). The support used to hold the sample in place was designed by following the instructions given by the standard BS ISO 18352, shown in Fig. 1(b).

The weight impact energy is equivalent to $m \times g \times h$, where m refers to impact mass, here 2.281kg was used, $g = 9.8m/s^2$ is gravitational acceleration, and h is the drop height. Impact energy is adjusted by changing the height of the drop-weight, details of which are shown in Table 1. The specimens were subjected to represent impact energies of 5, 10, 15, 20, 25 and 30J respectively. As shown in Fig.2 (a), in all samples, each of the damages are clearly visible from the impacted side, but they are hidden or less obvious from the rear surface, as shown in Fig. 2 (b).

Table 1: Drop height and impact energy level.

Specimen No.	Drop Height (m)	Energy Level (J)
#1	0.22	5
#2	0.45	10
#3	0.67	15
#4	0.89	20
#5	1.12	25
#6	1.34	30

2.2 Data collection

The experiment was conducted with the Thermoscope® II, a proprietary pulsed-active

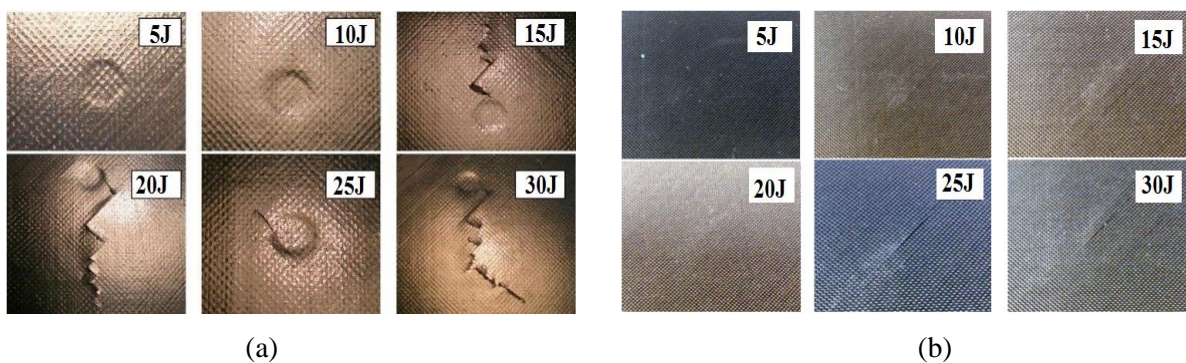


Fig. 2: Snapshot of 6 studied specimens. (a) Impact damage is visible from the impacted side of the specimens; (b) the rear surface of the samples present invisible or subtle evidence of damage.

thermography system from Thermal Wave Imaging Inc. This system comprises of two Xenon flash lamps mounted in an internally reflective hood with a capacitor bank providing power, and a desktop PC to capture and store data [28, 13]. A FLIR SC7000 series infrared radiometer was used, which has an Indium Antimonide (InSb) sensor with a spectral range of 3-5.1 μ m. The radiometer has a full spatial resolution of 640x512 pixels. The samples were placed with their surface perpendicular to the camera's line of sight at a distance of 300mm from the lens. Considering the thickness of the specimens and their low thermal diffusivity, a sampling rate of 25Hz was used.

2.3 Temperature decay curve

In pulse thermography, a short and high energy light pulse is projected onto the sample surface. The surface absorbs the light energy and its temperature increases. This heat is conducted through the sample, propagating inside the material causing a decrease in surface temperature. The surface temperature for a plate with a defect at a depth L is given by [29]

$$T(t) = \frac{Q}{\sqrt{\pi\rho ckt}} \left[1 + 2 \sum_{n=1}^{\infty} R^n \exp\left(-\frac{n^2 L^2}{\alpha t}\right) \right] \quad (1)$$

where $T(t)$ is the temperature of the surface at time t , Q is pulse energy, ρ is density, c is heat capacity, k is the thermal conductivity of material, α is thermal diffusivity and R is the thermal reflection coefficient of the air gap interface. For a semi-infinite medium, the temperature difference has a linear relation with time in the logarithmic domain with a slope of -0.5 [30].

The temperature response of any change in thermal material property from structure, damage or defect will deviate from the linear response. Shepard [17] proposed a Thermal Signal Reconstruction (TSR) technique to reduce temporal noise using a high order polynomial model to fit the temperature cooling curve. The model can be written as

$$\ln(T(t)) = \sum_{i=0}^N a_i (\ln(t))^i \quad (2)$$

where N is the model order and a_i are coefficients to be estimated. Normally, N is larger than 5. Once the unknown coefficients a_i are estimated by the least square method, the temperature behaviour can be reconstructed to replace the raw data. Noise is significantly reduced in TSR data and damages can then be better visualised. The first and second derivative of the fitting curve can be easily calculated by using the coefficients directly, and they have been proposed to determine the damage depth [30].

Fig. 3(a) shows an infrared image of the laminate that was subjected to an impact of 30J, where 'jet' colour map was used. Three pixels from different areas were considered and corresponding temperature decay curves in the logarithmic scale are shown in Fig. 3(b). It is shown that when the heat diffuses through the sound area (represented by red curve and marked by red cross in Fig. 3 (a)) the temperature decay characteristics are uniform for a slope of -0.5 as established in [30]. However, it can be inferred from the thermogram that there is the area represented by the green marker that shows a different temperature decay profile in comparison with the area where the material is not supposed to have any damage.

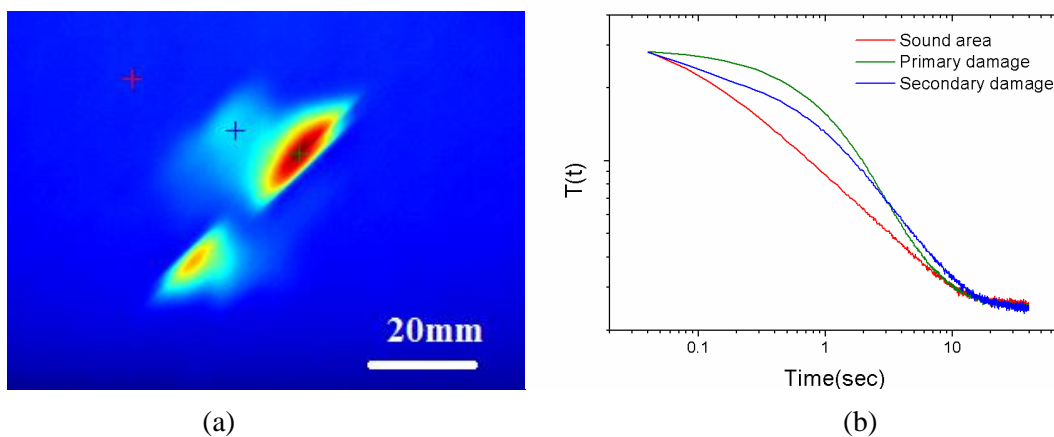


Fig. 3: (a) Infrared image of the laminate as shown in Fig.2 for 30J impact, inspected from the non-impact side of the laminate. This snapshot was sampled at 1 second after the flash, where the 'jet' colour map was used. (b) The logarithmic time-temperature curve plotted for three selected pixels in (a) with the marker colours indicating the respective curves.

This profile when plotted over time is represented by the green curve in Fig. 3(b), which confirms this deviation from the time-temperature profile of a sound area, confirming the presence of near and sub-surface damage as established in the literature [11, 12, 14, 31]. From Fig. 3(a), it can also be inferred that there is a secondary damage that has also been caused by the impact, but have a much lower contrast. It can be inferred that the deviation of the curve, now represented by the blue curve, from the base material (the red curve) confirms the presence of additional damage, which in this case may be referred to as secondary damage. The results obtained thus provide validation ensuring that the trend obtained is in line with what has been established in other researches.

3. Coefficient Clustering Analysis (CCA)

Fitting a high order polynomial model can be time consuming depending on the spatial resolution of images and the number of frames to be analysed. It also can cause over-fitting when the polynomial model describes noise instead of the underlying relationship [32]. Overfitting generally occurs when a model is excessively complex, such as having too many parameters relative to the number of observations. If a relatively low number of data are sampled, over-fitting can affect the performance of a high order model and this problem will be further amplified when using the first and second derivative. To address this issue, this paper proposes a new method to rapidly detect damaged areas using a second order polynomial model, which can be written as:

$$\ln(T(t) - T_0) = a_0 + a_1 \ln(t) + a_2 \ln(t)^2 \quad (3)$$

Although the model fitting is not as close as a high order model, the coefficients are much less sensitive to noise and more consistent for pixels from sound area. This fact is clearly evidenced by Fig. 4, where Fig. 4(a) shows the box chart for the polynomial coefficients a_1 with different model orders estimated from a damage-free specimen, and Fig. 4(b) shows the

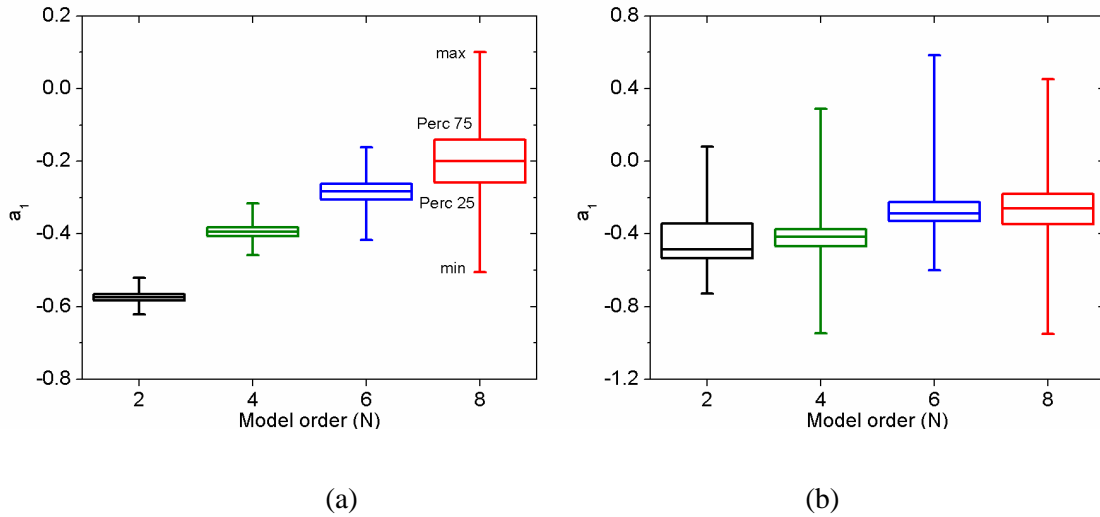


Fig. 4: Box chart for a_1 with different model orders estimated from a damage-free specimen (left) and a damaged specimen of 30J (right).

box chart for a_1 with different model orders estimated from a damaged specimen (30J). It can be observed from Fig. 4(a) that the variance of a_1 indicates the sensitivity to variation of pixels from the damage-free specimen, and its significant increase following the increment of the model order. As before, Fig. 4(b) represents the variation a_1 for a damaged area, indicating the sensitivity to variation of pixels. No significant difference has been observed between different model orders.

A novel coefficient clustering analysis (CCA) is introduced in this paper to explore the inner-relationship between coefficients to characterise and classify the thermal behaviour of each pixel of captured thermal images. Considering a damage-free specimen, an area of $100 \times$

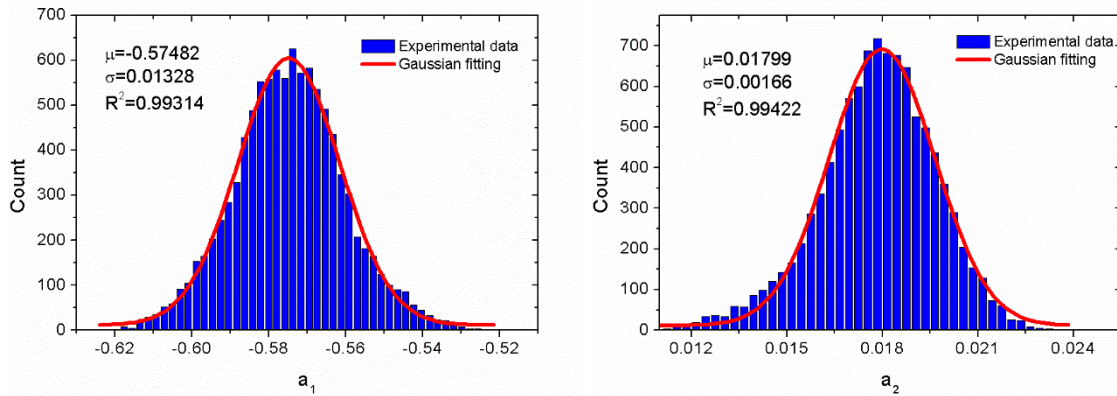


Fig. 5: The distribution of the coefficients for the damage-free specimen with corresponding Gaussian fitting.

100 pixels was sampled and the model (4) was fitted for each pixel. Fig. 5 shows the distribution of the first order coefficient a_1 and the second order coefficient a_2 with corresponding Gaussian fitting respectively. It is clearly shown that both coefficients are located within a narrow range with an approximate Gaussian distribution. The standard deviation of the fitting, σ , is 0.01328 and 0.00166 respectively, which is relatively very small comparing with the mean of distribution, μ , which is -0.57482 and 0.01799 respectively. The value of R-Square, as the indicator of approximation level, is 0.99314 and 0.99422, respectively.

Table 2: The parameters of the Gaussian fitting for the distribution of the first and second order coefficients for the 6 specimens, reflecting data extracted from ‘sound’ areas.

Specimen	a_1		a_2	
	Mean	Standard Deviation	Mean	Standard Deviation
5J	-0.57466	0.01241	0.01807	0.00146
10J	-0.56968	0.01422	0.01813	0.00196
15J	-0.56692	0.01546	0.01090	0.00103
20J	-0.56713	0.01566	0.01090	0.00102
25J	-0.55683	0.01573	0.01397	0.00180
30J	-0.54458	0.01163	0.01116	0.00177

To investigate the variance of coefficients across different samples, the above step was repeated for all specimens and the mean and standard deviation of Gaussian fitting for both coefficients of sound areas from each sample are shown in Table 2. The statistics results of the mean of a_1 (-0.5633 ± 0.0107) and a_2 (0.01385 ± 0.00349) clearly demonstrate the consistency of thermal behaviour for sound areas. On assessing sound area data, it has been observed that the first order coefficient increases following the increment of impact energy, which provides an indication that the impact event may have led to an overall change in the thermal behaviour of the sound area. All these observations reveal the potential to use both coefficients as the feature to classify sound and damaged pixels. This paper proposes to use the clustering between a_1 and a_2 as the base to perform classification.

Fig. 6 shows the scatter plot, illustrated by blue dots, for pixels sampled from the damage-free specimen. The plot exhibits a spindle shaped profile which indicates a strong linear relationship between these two coefficients. The linear relationship can be described as

$$a_2 = b_0 + b_1 a_1 \quad (4)$$

where b_0 and b_1 are intercept and slope to be estimated respectively. This model along with the boundary condition defines the constraint of a_1 and a_2 ($a_1 \in [\tau_1, \tau_2]$) of pixels from

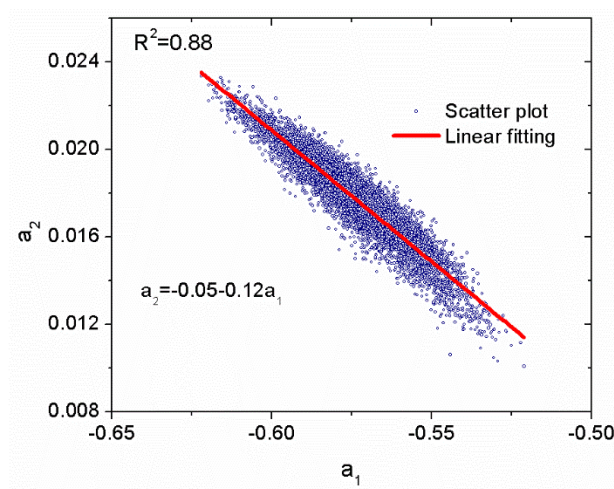


Fig. 6: The plot of the second order coefficient a_2 as a function of the first order coefficient a_1 for one damage-free specimen.

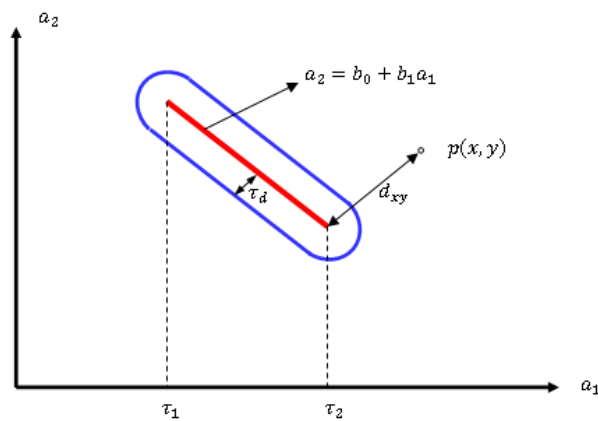


Fig. 7: Illustration of the classification process, where the red line segment denotes the baseline. Any pixel whose scatter of a_1 vs a_2 locates inside the region surrounded by the blue curve is determined as a pixel from sound area, or it is determined as a pixel from damaged area.

sound areas. The classification process is illustrated in Fig. 7, where the red line segment denotes the model (4). Considering a pixel $p(x, y)$, the first step is to estimate the first and second order coefficient of the model (3), and then calculate the shortest distance from the coefficient coordinate $(a_1^{x,y}, a_2^{x,y})$ to the line segment, denoted by d_{xy} . If d_{xy} is smaller than a preset tolerance τ_d , this pixel is determined as a pixel coming from a sound area of the component, or the pixel is determined as a damaged pixel. The value of d_{xy} indicates the level of difference of thermal behavior with damage free area. The larger the value of d_{xy} , the more complex the thermal behavior is, which could directly relate to the level of structure change. The value of τ_d is chosen based on the standard derivation of the coefficients calculated from the damage-free specimen. Through a large amount of testing and performance comparison, the paper proposes to select τ_d by

$$\tau_d = 2.5\sqrt{\sigma_1^2 + \sigma_2^2} \quad (5)$$

where σ_1 and σ_2 denotes the standard deviation of a_1 and a_2 , respectively.

Note the values of the parameters depend on the material and thickness of specimens. The identified model is applicable for components with the same material and thickness, any change of which requires re-calibrating the parameters using a reference sample or an area known as damage-free.

The steps of the proposed CCA method can be summarised as:

- 1) Select a region of a damage-free specimen, and estimate the baseline coefficients of model (3): a_0 , a_1 and a_2 ;
- 2) Fit the model (4) to estimate b_0 , b_1 based on the scatter plot of a_1 and a_2 , as shown in Fig. 6; Determine the boundary condition τ_1, τ_2 , and tolerance τ_d by estimating the distribution of the coefficients, as shown in Fig. 5;

- 3) Select a region of interest for a testing specimen, and estimate the coefficients of model (3): a_0 , a_1 and a_2 ;
- 4) Calculate the shortest distance from the coefficient coordinate $(a_1^{x,y}, a_2^{x,y})$ of each pixel to the baseline, as shown in Fig.7. If d_{xy} is smaller than τ_d , this pixel is determined as a pixel coming from a sound area, or the pixel is determined as a damaged pixel.
- 5) Visualise the damage by reversing pixels to space domain in a black-white form (Fig. 10) or color form (Fig. 12).

4. Results and Discussion

4.1 Damage detection

A region with a size of 200×200 pixels around the center of the specimen was sampled for all specimens. The unknown parameters for the model (4) were estimated from the reference sample and the model is finally expressed as

$$a_2 = -0.05 - 0.12a_1 \quad (6)$$

As shown in Fig. 6, the red plot illustrates the model (6) with $R^2 = 0.88$. The boundary condition of a_1 is determined by 99% quantile of distribution, which is $[-0.62, -0.53]$. The distance tolerance τ_d is chosen as 0.033 based on Eq. (5).

By applying the developed CCA method with the estimated parameters into the thermal decay data, the scatter plots of a_1 vs a_2 are shown in Fig. 8. The green scatters were classified as the pixels from sound areas, and the red scatters were classified as the pixels from damaged areas based on the process shown in Fig. 7.

There are almost no damaged pixels detected for the specimen at 5J. As expected, the number of damaged pixels detected increases following the increment of impact energy, which indicates a growing area of damage. The change in the contour of clustering indicates that a

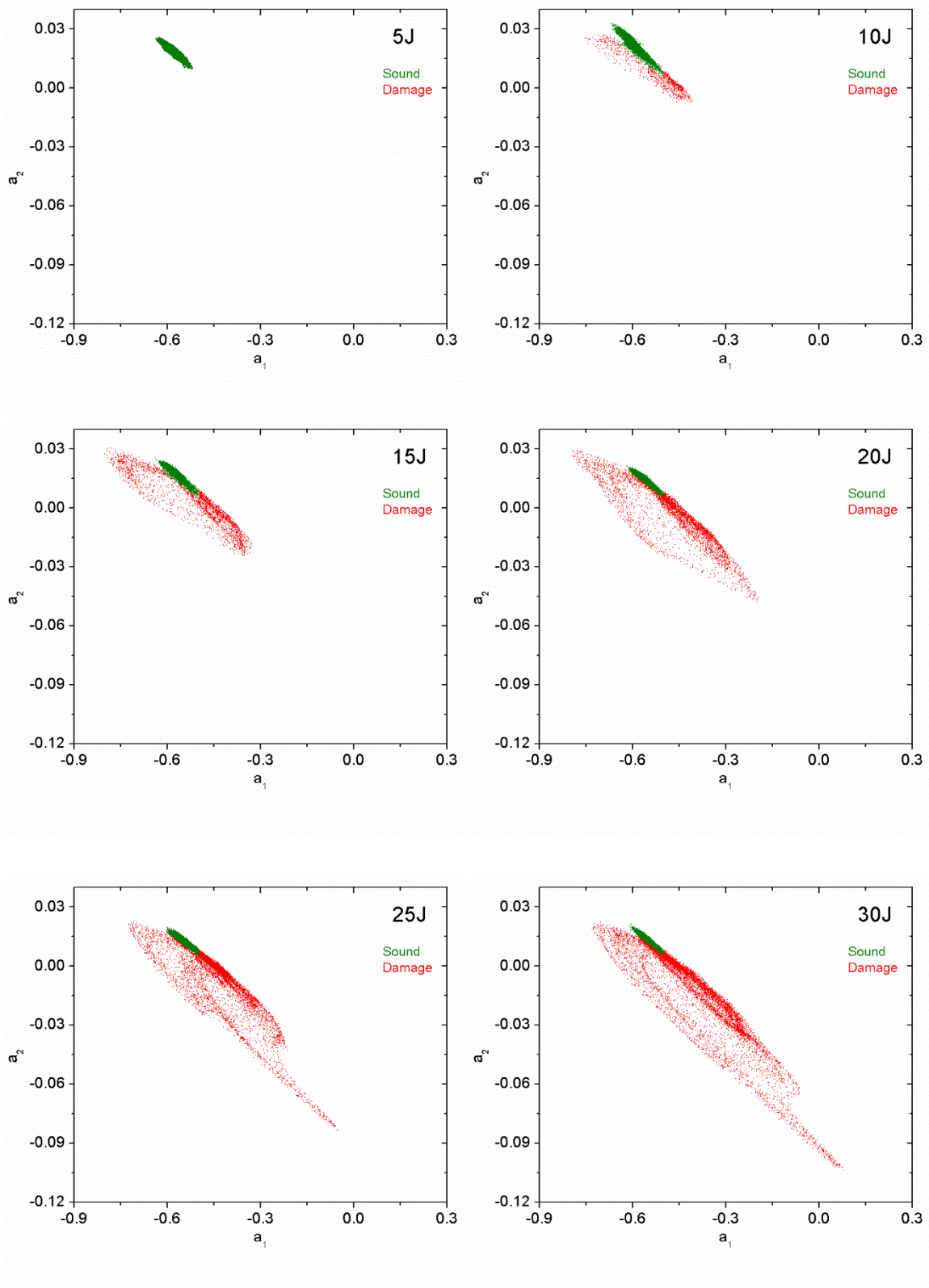


Fig. 8: The classification results based on the scatter of the first order coefficient and the second order coefficient for all specimens, where the green colour denotes the detected sound pixels and the red colour denotes the detected damaged pixel.

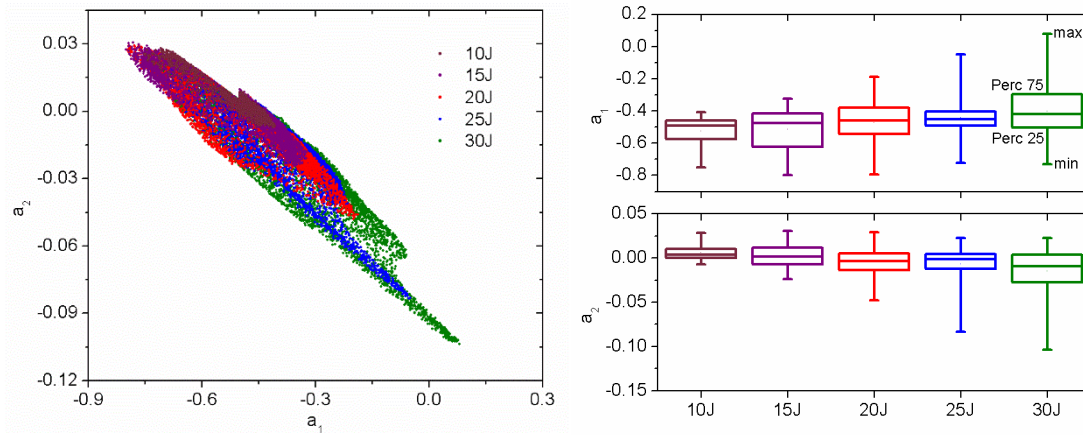


Fig. 9: Properties for pixels from defective areas for the specimen 10J-30J. Left: coefficient clustering overlay; top-right: box chart of the first order coefficient; bottom-right: box chart of the second order coefficient, which shows the minimum, maximum, 25% percentile and 75% percentile of all of the data.

higher energy impact causes more complex thermal behavior indicating potentially a more complex structural damage, which adds to deviation in the thermal behavior exhibited on the surface in comparison to sound areas. To explore more information, the left figure of Fig. 9 illustrates the overlap of coefficient clustering for pixels from defective areas for the specimen 10J-30J (5J is not included due to no damage detected). It has been observed that the scatters grow towards to the bottom-right corner following the increase of impact energy. This indicates that the linearity of temperature decay curve reduces because a_1 is closer to zero, and more complicated thermal behaviors have been observed because a_2 is further away from zero. The set of figures on the right in Fig. 9 show the box charts of both coefficients for pixels from damaged areas. It has been observed that following the increase of impact energy, the range between the maximum and the minimum for both coefficients increases which indicates that a higher energy impact potentially causes more complex structural damage. The minimums of a_1 are similar for all tests, but the maximum is closer to zero; the maximums of a_2 are similar for all tests, but the minimum is further away from zero. The variation of the box size for all tests is relatively small, which indicates that most damaged pixels have similar thermal behavior.

4.2 Damage measurement

Fig. 10 shows the visualisation of the detected damage area (black colour) in the binary form by converting the classification results into the spatial domain. To quantify the measurement, Table 3 presents the calculated properties of the detected damage area for each specimen, where the compactness measures the shape. Compactness was calculated by

$$compactness = \frac{4\pi \times area}{perimeter^2} \quad (7)$$

The value of the compactness is not greater than 1. If the shape of the area is a circle, the value of compactness arrives its maximum 1. Table 3 shows that the higher impact energy, the larger the area and perimeter of the detected damage is. It can be observed that the damaged area of the specimen 30J is smaller than 25J, but the perimeter is larger than 25J, which indicates a more irregular shape. This observation is confirmed by inspection of the compactness. The value of compactness for 10J, 15J, 20J and 25J is similar (mean: 0.634,



Fig. 10: Visualisation of the detected defect area for all specimens in the binary form.

Table 3: The property measures for the detected damage areas for all specimens.

Specimen	Area (mm ²)	Perimeter (mm)	compactness
10J	154.92	58.19	0.575
15J	397.08	86.60	0.665
20J	648.84	111.18	0.667
25J	1347.36	163.85	0.630
30J	1283.04	181.51	0.489

standard derivation: 0.043). The compactness of 30J is significantly smaller with the value of 0.489, which indicates a more irregular shape. A plot of perimeter as a function of impact energy, shown in Fig. 11, indicates a highly linear relationship. A line is fitted to the plot by the least square method with R^2 (coefficient of determination) = 0.97. For the specimen 30J, the high impact energy causes a potentially more complex damage structure, rather than an increased damage area in comparison with that of the 15J specimen.

Once the raw data sequence is converted into polynomial coefficients, and has undergone the coefficient clustering step transforming them into d_{xy} , these values can then be plotted back in the spatial domain, providing a new and alternative visualisation of the detected damage areas, as can be seen in Fig. 12. It has been observed that there are consistently two areas (top right

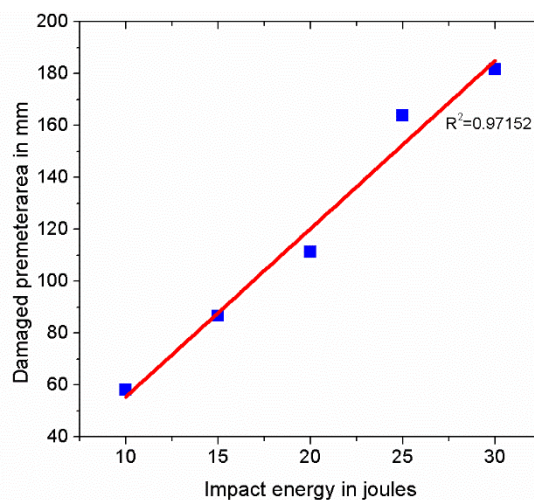


Fig. 11: Perimeter of the detected damaged area as a function of impact energy.

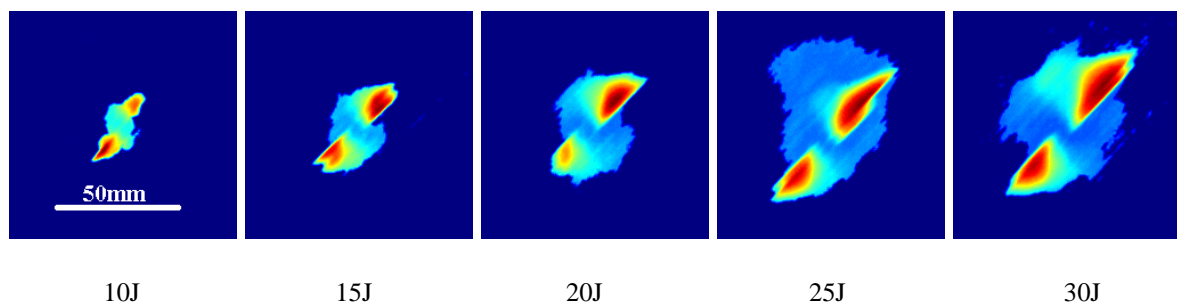


Fig. 12: Reconstructed data visualisation of damage across a range of samples: based on the d_{xy} values from the CCA method.

and bottom left) that have high values of d_{xy} for all specimens with impact damage. This phenomenon may be caused by the mechanism of the weight-drop machine itself.

5. Conclusions

Quantitative measurement of defective areas by pulse thermography has been an important research topic over the last decade. A high order polynomial model is normally used in existing methods to better fit the experimental data. However, over-fitting generally occurs when the number of observations are limited or the model is complex. To avoid this problem, this paper has developed a novel coefficient clustering analysis method based on a second order polynomial fitting for the temperature decay curve. It has been observed that the estimated coefficients of sound pixels exhibit an approximate Gaussian distribution, and the variance of both coefficients for different testing specimens is relatively small. The clustering of coefficients is therefore selected as a feature to represent the thermal behavior of each pixel. A simple linear function describing the relationship between two coefficients with a corresponding boundary condition has been developed to classify pixels from damaged and sound areas of the specimens.

The evaluation of the performance and accuracy of the proposed CCA method are based on experimental data from carbon fibre laminates that suffered different impact energies. Clustering results reveal that the higher the impact energy, the wider the distribution of the scatter plot of damaged pixels; indicating a more complex thermal behaviour. Both binary and colour visualisations show that the higher the impact energy, the more complex the thermal behaviours it causes. It has been observed that the specimen with 30J impact has a more irregular shape than other 5 specimens. The perimeter of the detected area and the impact energy exhibits a highly linear relationship. Analysis of the results reveals clear potential of the new CCA method.

It should be inferred from the reverted spatial images that they don't just represent a single frame from the dataset, as represented by other existing methods; but represent the reconstruction of the entire dataset compressed into a single image. This technique not only provides an enhanced visual confirmation of the damage, but also reduces the burden on the operator in post-processing the data.

The present study can only detect and measure damage size. Future research will be focused on the development of an efficient coarse-to-fine damage assessment routine, which would perform a rapid inspection, initially identifying the damaged areas based on CCA to provide the reference point for sound material. From this, the region of interest can be deduced, allowing depth measurement techniques to then be applied to the identified areas.

Acknowledgements

The authors would like to thank Professor Peter Foote from Cranfield University for providing the CFRP specimens. This work was supported by the EPSRC Centre for Innovative Manufacturing in Through-life Engineering Services (Grant number EP/I033246/1).

References

- [1] Boeing, "Boeing 787 from the Ground Up," BOEING, 2006.
- [2] U. Polimeno and M. Meo, "Detecting barely visible impact damage detection on aircraft composites structures," *Composite Structures*, vol. 91, no. 4, p. 398–402, 2009.
- [3] "Civil Aircraft Airworthiness Information and Procedures (CAAIP)," Authority Civil Aviation, 2013.

- [4] G. Newaz and R. Sierakowski, *Damage tolerance in advanced composites*, CRC Press, 1995.
- [5] S. Sanchez-Saez, E. Barbero, R. Zaera and C. Navarro, "Compression after impact of thin composite laminates," *Composites Science and Technology*, vol. 65, no. 13, p. 1911–1919, 2005.
- [6] M. Freitas and L. Reis, "Failure mechanisms on composite specimens subjected to compression after impact," *Composite Structures*, vol. 42, p. 365–373, 1998.
- [7] M. Jadin and S. Taib, "Recent progress in diagnosing the reliability of electrical equipment by using infrared thermography," *Infrared Physics & Technology*, vol. 55, p. 236–245, 2012.
- [8] S. Bagavathiappan, T. Saravanan, N. George, J. Philip and R. T. Jayakumar, "Condition monitoring of exhaust system blowers using infrared thermography," *Insight*, vol. 50, p. 512–515, 2008.
- [9] C. Meola, G. Carlomagno, A. Squillace and G. Giorleo, "The use of infrared thermography for nondestructive evaluation of joints," *Infrared Physics & Technology*, vol. 46, p. 93–99, 2004.
- [10] E. Grinzato, C. Bressan, S. Marinetti, P. Bison and C. Bonacina, "Monitoring of the Scrovegni Chapel by IR thermography: Giotto at infrared," *Infrared Physics & Technology*, vol. 43, p. 165–169, 2002.
- [11] V. Vavilov, X. Maldague, B. Dufort, F. Robitaille and J. Picard, "Thermal nondestructive testing of carbon epoxy composites: detailed analysis and data processing," *NDT & E International*, vol. 26, no. 2, p. 85–95, 1993.

- [12] R. Ball and D. Almond, "The detection and measurement of impact damage in thick carbon fiber reinforced laminates by transient thermography," *NDT & E International*, vol. 31, no. 3, pp. 165-173, 1998.
- [13] J. Mehnen, L. Tinsley and R. Roy, "Automated in-service damage identification," *CIRP Annals - Manufacturing Technology*, vol. 63, no. 1, pp. 33-36, 2014.
- [14] C. Ibarra-Castanedo, A. Bendada and X. P. V. Maldague, "Thermographic Image Processing for NDT," *IV Conferencia Panamericana de END*, pp. 1-12, 2007.
- [15] X. Maldague, *Theory and practice of infrared technology for nondestructive testing*, New York: Wiley, 2001.
- [16] C. Ibarra-Castanedo, A. Bendada and X. Maldague, "Image and signal processing techniques in pulsed thermography," *GESTS Int'l Trans. Computer Science and Engineering*, vol. 22, no. 1, pp. 89-100, 2005.
- [17] S. M. Shepard, "Temporal noise reduction, compression and analysis of thermographic image data sequences". US Patent 6516084 B2, 2003.
- [18] N. Rajic, "Principal component thermography for flaw contrast enhancement and flaw depth characterisation in composite structures," *Composite Structures*, vol. 58, no. 4, pp. 521-528, 2002.
- [19] H. Schmutzler, A. Garcia, N. Sato, H. Wittich, M. Nishikawa, H. Rohling, M. Hojo, K. Schulte and B. Fiedler, "Influence of Delamination Characteristics in Carbon Fibre/Epoxy Laminates on Signal Features of Pulse Thermography," *Journal of Nondestructive Evaluation*, vol. 34, no. 1, 2014.
- [20] F. J. Madruga, C. Ibarra-Castanedo, O. Conde, J. López-Higuera and X. Maldague,

“Automatic data processing based on the skewness statistic parameter for subsurface defect detection by active infrared thermography,” in *9th International Conference on Quantitative InfraRed Thermography*, Krakow, Poland, 2008.

[21] F. J. Madruga, C. Ibarra-Castanedo, O. M. Conde, J. M. López-Higuera and X. Maldague, “Infrared thermography processing based on higher-order statistics,” *NDT & E International*, vol. 43, no. 8, pp. 661-666, 2010.

[22] J. Roche, F. Leroy and D. Balageas, “Information condensation in defect detection using TSR coefficients images,” in *The 12th International Conference on Quantitative InfraRed Thermography*, 2015.

[23] J. M. Roche, F. Passilly and D. Balageas, “TSR-Based Quantitative Processing Procedure to Synthesize Thermal D-Scans of Real-Life Damage in Composite Structures,” *Journal of Nondestructive Evaluation*, vol. 34, no. 4, pp. 1-15, 2015.

[24] H. I. Ringermacher, R. J. Archacki and W. A. Veronesi, “Nondestructive testing: Transient depth thermography”. US Patent 5711603, 1998.

[25] S. M. Shepard, “Automated binary processing of thermographic sequence data”. US Patent 8449176 B2, 2003.

[26] J. Sun, “Analysis of pulse thermography methods for defect depth prediction,” *Journal of Heat Transfer*, vol. 128, pp. 329-338, 2003.

[27] J. G. Sun, “Method for Determining Defect Depth Using Thermal Imaging”. U.S. Patent 6,542,849, 2003.

[28] T. Widjanarko, L. Tinsley, R. Roy and J. Mehnen, “Characterisation and performance assessment of a pulsed-thermography camera system for component degradation

inspection,” in *Proceedings of the 1st International Conference on Through-life Engineering Services*, Cranfield, UK, 2012.

- [29] S. Lau, D. Almond and J. Milne, “A quantitative analysis of pulsed video thermography,” *NDT & E International*, vol. 24, no. 4, pp. 195-202, 1991.
- [30] S. M. Shepard, J. Hou, J. R. Lhota and J. M. Golden, “Automated processing of thermographic derivatives for quality assurance,” *Optical Engineering*, vol. 46, no. 5, p. 051008, 2007.
- [31] S. M. Shepard, “Advances in Pulsed Thermography,” *Processings of SPIE*, vol. 4360, pp. 511-515, 2011.
- [32] K. Chana, C. Kwongb, T. Dillona and Y. Tsim, “Reducing overfitting in manufacturing process modeling using a backward elimination based genetic programming,” *Applied Soft Computing*, vol. 11, p. 1648–1656, 2011.
- [33] W. J. Parker, R. J. Jenkins, C. P. Butler and G. L. Abbott, “Flash Method of Determining Thermal Diffusivity, Heat Capacity, and Thermal Conductivity,” *Journal of Applied Physics*, vol. 32, p. 1679–1684, 1961.